

Continuum emission around AGB stars at 1.2 mm^{*}

S. Dehaes^{1†‡}, M.A.T. Groenewegen¹, L. Decin¹, S. Hony², G. Raskin¹
and J.A.D.L. Blommaert¹

¹ *Institute for Astronomy, University of Leuven, Celestijnenlaan 200D, 3001 Leuven, Belgium*

² *Service d'Astrophysique, Bat.609 Orme des Merisiers, CEA Saclay, 91191 Gif-sur-Yvette, France*

Accepted . Received ; in original form

ABSTRACT

It is generally acknowledged that the mass loss of Asymptotic Giant Branch (AGB) stars undergoes variations on different time scales. We constructed models for the dust envelopes for a sample of AGB stars to assess whether mass-loss variations influence the spectral energy distribution (SED). To constrain the variability, extra observations at millimetre wavelengths (1.2 mm) were acquired. From the analysis of the dust models, two indications for the presence of mass-loss variations can be found, being (1) a dust temperature at the inner boundary of the dust envelope that is far below the dust condensation temperature and (2) an altered density distribution with respect to $\rho(r) \propto r^{-2}$ resulting from a constant mass-loss rate. For 5 out of the 18 studied sources a two-component model of the envelope is required, consisting of an inner region with a constant mass-loss rate and an outer region with a less steep density distribution. For one source an outer region with a steeper density distribution was found. Moreover, in a search for time variability in our data set at 1.2 mm, we found that WX Psc shows a large relative time variation of 34% which might partially be caused by variable molecular line emission.

Key words: Stars: AGB and Post-AGB – stars: mass-loss – stars: variables: other – radio continuum: stars.

1 INTRODUCTION

When low- and intermediate mass stars enter the AGB phase at the end of their lives, the mass-loss rate exceeds the nuclear burning rate and so dominates the subsequent evolution. In this process, a circumstellar envelope (CSE) of gas and dust is formed which expands at a rate of about 10 km s^{-1} (see for example Habing (1996)).

The AGB mass loss undergoes variations on different time scales. The mass loss gradually increases over a time scale of several hundred thousands of years to reach a maximum on the tip of the Thermally Pulsing-AGB (Habing 1996). The pulsations of the central star cause variations over several hundreds of days. Strong variations in the mass-loss rate, probably related to thermal pulses occurring every 5-10 10^4 yr (Vassiliadis & Wood 1993), can lead to the formation of circumstellar detached shells. Schöier, Lindqvist & Olofsson (2005) have recently studied 7 car-

bon stars with known detached molecular shells. They find that the shells are caused by periods of very intense mass loss ($\sim 10^{-5} \text{ M}_{\odot} \text{ yr}^{-1}$) and that these shells are running into a previous low mass-loss-rate AGB wind. After the intense mass-losing period, the mass loss decreases to a few $10^{-8} \text{ M}_{\odot}$, on a time scale of a few thousand years.

The question then arises if these types of mass-loss variations can be deduced from the SED. To answer this question, we modelled the SED of a carefully selected sample of nearby AGB stars, post-AGB stars and supergiants. For modelling purposes it proved desirable to obtain millimetre observations of the stars in our sample, as there are not many observations available in the literature in this wavelength range. Still, a considerable part of the dust envelope is so cold that it emits its radiation at millimetre wavelengths, making these fluxes necessary to constrain the models for the SEDs.

The outline of this article is as follows. First, the obtained fluxes at 1.2 mm are presented. Sect. 2 contains information on the sample selection, the observations with SIMBA and the data reduction with MOPSI. Sect. 3 is devoted to the aperture photometry. In Sect. 4 the constructed models for the SEDs are presented and the quality of these

^{*} Based on observations collected at the European Southern Observatory, La Silla, Chile within program ESO 70.D-0133, 71.D-0072 and 71.D-0600.

[†] Scientific researcher of the Fund for Scientific Research, Flanders

[‡] E-mail: sofie@ster.kuleuven.be

models and the indications for variable mass loss are discussed. In Sect. 5, the variability at 1.2 mm is analysed on the basis of our observations. The conclusions are summarised in Sect. 6.

2 OBSERVATIONS AND DATA REDUCTION

2.1 Sample selection

The AGB stars in the sample include M- and C-stars. We have also observed some post-AGB stars and supergiants that are known to have circumstellar shells. To improve the sensitivity to very faint circumstellar emission, the selection was restricted to objects with low mm-background emission based on the *IRAS* 60 and 100 μm data (typically the CIRR3 flag, which is the total 100 μm sky surface brightness, $\leq 50 \text{ MJy sr}^{-1}$) and the sample was further restricted to stars within 1 kpc (see Table 3). There are a few exceptions, such as the unique F-type supergiant IRC +10420.

2.2 Observations

The data were taken with the 37-channel hexagonal bolometer array SIMBA installed at the 15-m SEST telescope, during 3 observation runs: 2002 September 5–10, 2003 May 9–13 and 2003 July 13–15. The channels have a half power beam width (HPBW) of 24 arcsec and two adjacent channels are separated by 44 arcsec. The filter bandpass is centered on 1.2 mm or 250 GHz and has a full width half max (FWHM) of 90 GHz.

SIMBA works without a wobbling secondary mirror; the maps were made with the fast-scanning technique. The scans were performed in azimuthal direction by moving the telescope at a speed of 80 arcsec s^{-1} with a separation in azimuth of 8 arcsec. The size of the scans varies between $500 \text{ arcsec} \times 360 \text{ arcsec}$ and $600 \text{ arcsec} \times 480 \text{ arcsec}$. 4 to 8 consecutive scans were made of each source. This procedure was repeated several times for each source during the observation runs. Although SIMBA has a hexagonal array design, there are still gaps in the spatial coverage. Because the telescope is set up in horizontal coordinates, the scan direction on the sky changes with the hour angle. By assembling scans taken at different hour angles, the gaps in the spatial coverage are reduced. Of course the assembling of the different scans also increases the signal-to-noise ratio.

2.3 Data reduction

The MOPSI software was used to reduce the data. Basically the procedure described in the section on MOPSI in the SIMBA user-manual (Observers handbook SIMBA 2003) was followed, but the reduction was further divided into 3 different steps. In the first step some fundamental operations like despiking, opacity correction and sky-noise reduction are performed on each of the individual scans. Also, the 4 to 8 consecutive scans of each source are put together to form one map. In a second step, the maps made during different nights are assembled. If the source was detected in the individual maps, the maps were recentered before the assembling. Out of this map information is gained about the

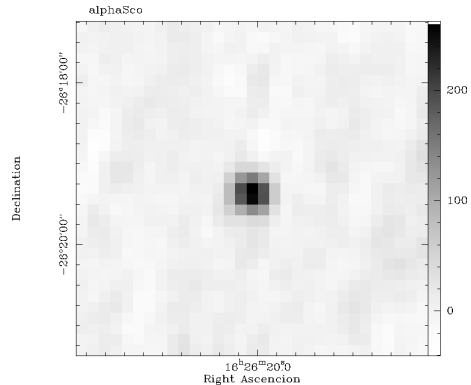


Figure 1. The final map of $\alpha \text{ Sco}$, resulting from the observations of September 2002. The legend is expressed in mJy, the rms-noise on the sky background is 27.7 mJy.

position of the source, which is used in the last step to define a proper baseline and to improve the sky-noise reduction.

For the absolute calibration, scans were made of Uranus, typically at the beginning and/or end of each observing night. The data reduction is basically the same as for the scientific sources, although a few steps were altered because Uranus is a relatively strong and extended source. Only low order baseline fits were used (with an appropriate base range definition) and neither despiking nor sky-noise reduction were carried out, as recommended in the manual. The flux of Uranus at 250 GHz was estimated with the subprogram ‘Planet’ in MOPSI. Table 1 gives the resulting calibration factors for the 3 observation runs. As an example, Fig. 1 shows the final map of $\alpha \text{ Sco}$ resulting from the observations of September 2002.

3 APERTURE PHOTOMETRY

After the data reduction, the fluxes were determined using aperture photometry. For each source we searched for the ‘ideal’ aperture: the aperture with the highest corresponding signal-to-noise ratio. For the small apertures a correction is necessary, because one neglects counts from the source that were detected outside the aperture. To apply this correction, the point spread function or PSF had to be determined.

The PSF was calculated using the 3 final maps of Uranus from the 3 observation runs. We used Uranus and not one of the scientific targets because it is such a strong source and its angular diameter is well known. Because it is an extended source, the maps do not just represent the PSF, but a convolution of the PSF with a uniform disk with diameter equal to the angular diameter of Uranus. As we wanted to model the PSF with a gaussian profile, we fitted a convolution of a uniform disk with an elliptic gaussian profile to each of the 3 maps and determined the best fit with a least-squares method. The variances in the x- and y-direction of the 3 resulting gaussian profiles are given in Table 1, together with the corresponding FWHM (which is $2\sqrt{2 \ln 2} \sigma$) in the 2 directions. The given uncertainties are 1σ errors. As can be seen from Table 1, there is little difference between the variances of the 3 gaussian fits. The variances of the average PSF were calculated as weighted averages of

Table 1. The first row gives the calibration factors for each of the observation runs. The rest of the table contains the variances of the gaussian profiles for the 3 observation runs and of the averaged PSF, together with the corresponding FWHM.

	Sep02	May03	Jul03	PSF
calibration factor (to mJy)	62.0 ± 2.6	64.5 ± 2.7	58.6 ± 2.4	
σ_x	10.44 ± 0.47	10.30 ± 0.45	10.49 ± 0.73	10.40 ± 0.30
σ_y	10.55 ± 0.48	9.92 ± 0.44	11.13 ± 0.78	10.43 ± 0.31
FWHM _x	24.7 ± 1.2 arcsec	24.3 ± 1.1 arcsec	24.7 ± 1.8 arcsec	24.49 ± 0.71 arcsec
FWHM _y	24.8 ± 1.2 arcsec	23.4 ± 1.1 arcsec	26.2 ± 1.9 arcsec	24.56 ± 0.73 arcsec

Table 2. The scale factors to correct for count loss within small apertures.

aperture	scale factor
40 arcsec	0.99946 ± 0.00014
35 arcsec	0.99658 ± 0.00068
30 arcsec	0.9841 ± 0.0023
25 arcsec	0.9438 ± 0.0054
20 arcsec	0.8419 ± 0.0095
15 arcsec	0.647 ± 0.012

σ_x and σ_y from the 3 fits, which are also given in Table 1. The corresponding FWHM in the x- and y-direction of the average PSF are in good agreement with the expected value of 24 arcsec, which is the HPBW of one channel.

With the help of the average PSF, the scale factors to correct for count losses with small apertures could be determined (see Table 2). An aperture of 45 arcsec already contains 99.99% of the flux, so we put the scale factors for apertures ≥ 45 arcsec equal to 1. The scale factors from the 3 individual gaussian fits were also calculated to determine the rms-errors on the scale factors from the average PSF.

Once these scale factors were known, we continued by determining the ideal aperture and the corresponding flux for each of the scientific targets. In the user manual of MOPSI one can find the commands to determine the number of counts within a given aperture, as well as the error. We have discovered that the numbers that MOPSI returns are not what we understand to be the number of counts and the error. MOPSI considers the number of positive counts in the integration area as the total number of counts and the number of negative counts as the error. Hence MOPSI adds the positive noise to the total number of counts, but neglects the negative noise. In our opinion it is better to take the positive counts minus the negative counts as the total number of counts, because after the data reduction one expects the noise to fluctuate around zero.

To calculate the error on this total number of counts, we assumed that the noise follows a Poisson distribution, so that the error equals the square root of the total number of counts. When the ideal aperture is less than 45 arcsec, a scale factor had to be applied to derive the total number: in that case the error on the scale factor propagates into the error on the counts. The total number of counts within the ideal aperture also has to be divided by the area of the PSF, Ω , being

$$\Omega = \frac{\text{FWHM}_x \text{FWHM}_y \pi}{4 \ln 2}$$

The values of FWHM_x and FWHM_y from the average PSF from Table 1 were used. The error on Ω , resulting from the errors on FWHM_x and FWHM_y, was also accounted for in the error on the total number of counts. Finally, we also took the error on the calibration factors into account (see Table 1).

To make sure that we do not exclude any extended emission by using the ideal aperture, we have fitted gaussian profiles to each of the detected sources. We have taken ideal apertures that contain at least 99% of the volume underneath those gaussian fits. Besides the gaussian flux profiles of the central sources, no other structures are visible in the maps, so there is no danger of contamination of the flux by other objects, not even for the largest apertures.

The resulting flux and the ideal aperture for each of the science targets are given in Table 3.

4 MODELLING OF THE SED

4.1 Methodology

For all 23 sources that were detected with SIMBA, models were constructed for the SED with DUSTY (Ivezić et al. 1999). DUSTY is a code that solves the problem of radiation transport in a dusty environment. Its input consists of four categories of parameters: information about the external radiation source, about the dust properties, the density distribution and the overall optical depth of the dust envelope. From this information, the code calculates the dust temperature distribution and the radiation field, by solving a self-consistent equation for the radiative energy density, including dust scattering, absorption and emission.

For the modelling of our sources, a spherical model was used, in which the external radiation comes from a point source at the centre of the density distribution. The spectral shape of the external radiation is determined by a black body of a given temperature. For the oxygen-rich dust envelopes, we used silicates to model the chemical composition of the CSE. DUSTY contains the optical properties of 3 types of silicates: hot and cold silicates which are discussed by Ossenkopf, Henning & Mathis (1992) and a silicate with optical constants from Draine & Lee (1984) (further abbreviated by SilOw, SilOc and SilDL). For the oxygen-rich envelopes, only models with one type of grain were tested, never a mixture. For the carbon-rich envelopes in our sample, a mixture with varying ratios of amorphous carbon (AMC, with optical constants from Hanner (1988)) and SiC (with optical constants from Pégourié (1988)) was used. The size of the grains was fixed at 0.1 μm . The inner radius of the dust envelope is fixed

Table 3. General information about the science targets, together with the derived flux and the corresponding ideal aperture. In case no detection was made, three times the rms on the sky background is given as an upper limit. A question mark in the column of the distances means that no reliable distance estimate was available. References are given below.

Name	RA	Dec	spectral type	distance (kpc)	observation run	flux at 1.2 mm (mJy)	ideal aperture (arcsec)	rms (mJy)
AFGL 1922	17 : 04 : 55.1	-24 : 40 : 41	C ^a	0.88 ^e	Sep02	93.7 ± 6.2	50	8.0
α Sco	16 : 26 : 20.3	-26 : 19 : 22	M1.5Iab-b ^b	0.19 ^f	Sep02	244.4 ± 15.1	35	9.2
α Sco					Jul03	237.9 ± 14.7	40	8.7
HD 44179	06 : 17 : 37.0	-10 : 36 : 52	B8V ^b	0.33 ^g	Sep02	356.1 ± 21.6	40	10.5
IRAS 15194-5115	15 : 19 : 27.0	-51 : 15 : 18	C ^a	0.6 ^h	Sep02	310.6 ± 19.0	65	9.8
o Cet	02 : 16 : 49.1	-03 : 12 : 13	M7IIIe ^b	0.11 ^e	Sep02	180.7 ± 11.3	55	8.0
AFGL 3068	23 : 16 : 42.4	16 : 55 : 10	C ^c	0.95 ^e	Sep02	429.4 ± 25.9	90	9.8
IK Tau	03 : 50 : 43.7	11 : 15 : 31	M6me ^b	0.26 ^e	Sep02	436.0 ± 26.3	115	8.6
IRC +10 420	19 : 24 : 26.7	11 : 15 : 09	F8Ia ^b	4 - 6 ⁱ	Sep02	460.7 ± 27.8	100	11.7
VY CMa	07 : 20 : 54.8	-25 : 40 : 12	M3/M4II ^b	0.66 ^e	Sep02	689.7 ± 41.2	60	10.5
WX Psc	01 : 03 : 48.1	12 : 19 : 51	M9 ^b	0.54 ^e	Sep02	328.3 ± 20.0	115	6.8
WX Psc					Jul03	158.1 ± 10.0	75	8.7
V1300 Aql	20 : 07 : 47.4	-06 : 25 : 11	M ^b	0.66 ^e	May03	103.4 ± 6.9	70	7.0
IRAS 08005-2356	08 : 00 : 32.6	-23 : 56 : 16	F5e ^b	?	Sep02	< 27.7		9.2
HD 56126	07 : 13 : 25.3	10 : 05 : 09	F5Iab ^b	2.3 ^j	Sep02	< 48.0		16.0
HD 56126					May03	< 51.8		17.3
S Sct	18 : 47 : 37.2	-07 : 58 : 00	C6,4(N3) ^d	0.62 ^e	Sep02	< 120.0		40.0
S Sct					May03	< 32.6		10.9
HD 187885	19 : 50 : 00.8	-17 : 09 : 38	F2/F3Iab ^b	?	Sep02	< 29.5		9.8
HD 187885					May03	< 23.0		7.7
HD 179821	19 : 11 : 25.0	00 : 02 : 19	G5Ia ^b	1 ^k	Sep02	< 79.4		26.5
HD 179821					May03	< 78.7		26.2
89 Her	17 : 53 : 24.1	26 : 03 : 23	F2Ibe ^b	0.98 ^f	May03	69.5 ± 4.8	50	9.6
AFGL 4106	10 : 21 : 32.4	-59 : 16 : 52	K0 ^b	3.3 ^l	May03	96.0 ± 6.4	60	9.6
IRC +10 216	09 : 45 : 14.9	13 : 30 : 40	C9,5 ^d	0.12 ^e	May03	3764.3 ± 221.4	70	12.2
IRC +20 326	17 : 29 : 42.5	17 : 47 : 27	C ^c	0.79 ^e	May03	8.9 ± 1.1	50	10.9
IRC +20 370	18 : 39 : 42.0	17 : 38 : 10	C ^b	0.60 ^e	May03	58.9 ± 4.2	50	16.0
R Hya	13 : 26 : 58.3	-23 : 01 : 25	M7IIIe ^b	0.13 ^e	May03	94.7 ± 6.3	30	12.8
V Hya	10 : 49 : 11.3	-20 : 59 : 04	C6,3e-C7,5e(N6e) ^d	0.33 ^e	May03	99.5 ± 6.6	35	7.7
W Hya	16 : 46 : 12.2	-28 : 07 : 07	M7IIIe ^b	0.12 ^e	May03	280.0 ± 17.2	45	7.7
CPD-56 8032	17 : 04 : 47.8	-56 : 50 : 56	WC ^b	1.35 ^m	May03	255.4 ± 15.8	100	8.3
IRAS 14331-6435	14 : 33 : 07.9	-64 : 35 : 03	B3Iab:e ^b	?	May03	94.2 ± 6.3	85	11.5
U Hya	10 : 35 : 05.0	-13 : 07 : 26	C6.5,3(N2) ^d	0.35 ^e	May03	< 30.7		10.2
HR 4049	10 : 15 : 49.9	-28 : 44 : 29	B9.5Ib-II ^b	0.67 ^f	May03	< 28.8		10.2
AC Her	18 : 28 : 09.0	21 : 49 : 53	F4Ibpvar ^b	0.75 ⁿ	May03	< 107.5		35.8
α Her	17 : 12 : 21.9	14 : 26 : 45	M5Iab ^b	0.12 ^e	Jul03	147.5 ± 9.4	45	9.3
R Scl	01 : 24 : 40.1	-32 : 48 : 07	C6,5ea(Np) ^d	0.47 ^e	Jul03	61.2 ± 4.3	35	4.1
TX Psc	23 : 43 : 50.1	03 : 12 : 34	C7,2(N0) ^d	0.23 ^e	Jul03	< 26.2		8.7

a = Groenewegen, de Jong & Baas (1993), b = SIMBAD, c = Kwok, Volk & Bidelman (1997), d = Samus et al. (2004), e = Loup et al. (1993), f = ESA (1997), g = Cohen et al. (1975), h = Ryde, Schöier & Olofsson (1999), i = Jones et al. (1993), j = Jura, Chen & Werner (2000a), k = Josselin & Lèbre (2001), l = Molster et al. (1999), m = de Marco, Barlow & Storey (1997), n = Jura, Chen & Werner (2000b)

by specifying the dust temperature at the inner boundary, DUSTY assumes instantaneous dust formation at this radius. When dealing with objects where the expansion of the envelope is driven by radiation pressure on dust grains, DUSTY can compute the density structure in the envelope by solving the hydrodynamics equations, coupled to the radiative transfer equations. In this case, the only input parameter required is the relative extension of the dust shell in comparison to the inner radius: this parameter was fixed at 5000 (resulting in a dust temperature at the outer boundary of the dust shell of about 30 K, to meet the temperature of the interstellar medium). In these calculations, DUSTY assumes a luminosity of $10^4 L_{\odot}$, a gas-to-dust mass ratio of 200 and a dust grain bulk density of 3 g cm^{-3} .

To construct the SEDs, photometric data were collected from the astronomical database VizieR and from a report by van der Hucht (2004, private communication) that lists photometric data from the literature between $12 \mu\text{m}$ and 6 cm for about half of the sources in our sample. To further constrain the model, we made use of the *IRAS* low-resolution spectrometer spectra with wavelengths between 8 and $23 \mu\text{m}$ (obtained from the website http://www.iras.ucalgary.ca/~volk/getlrs_plot.html). To estimate the interstellar reddening, a program based on the model of Arenou, Grenon & Gomez (1992) was used. Every model that was tested, was reddened according to the average interstellar extinction law for the Johnson system from Savage & Mathis (1979).

As a starting point, a model with an effective temperature of 2500 K and an optical depth at $0.5 \mu\text{m}$ of 10 was taken, with a dust temperature at the inner boundary of the dust envelope of 1000 K. For a carbon-rich envelope we started out with a chemical composition with 90% amorphous carbon and 10% SiC, for an oxygen-rich envelope SiIDL was tried first. Ivezić & Elitzur (1997) have made an extensive parameter study from which the influence of each input parameter on the shape and scale of the SED becomes clear. We have done a parameter study ourselves in a smaller parameter space, especially to study the influence of the different parameters on the predicted LRS spectrum, which is not clear from the SEDs presented in Ivezić & Elitzur (1997).

Starting from the model described above, the parameters T_{eff} , $\tau_{0.5}$, T_1 and the chemical composition were altered to improve the fit as follows. First the optical depth is adjusted since this parameter has the largest influence on the model out of the four mentioned above. It does not change the overall shape of the SED, a larger optical depth merely shifts the complete SED redwards. Then the chemical composition is determined. For a carbon-rich envelope, the strength of the $11.3 \mu\text{m}$ feature increases as the percentage of SiC is increased. Concerning the oxygen rich case, the type of silicate is determined by the relative strength of the $9.7 \mu\text{m}$ and $18 \mu\text{m}$ features. Since the strength of the features is also strongly dependent on the value of $\tau_{0.5}$, the silicate features can put additional constraint on this parameter as well. The effective temperature of AGB sources typically lies between 2000 and 3500 K. Since this is a small temperature range, the effects on the SED are also relatively small. T_{eff} affects the shape of the SED blueward of the peak of the energy distribution and only has a minor scale effect redwards of the peak. T_{eff} only plays a role in the SED when $\tau_{0.5} \leq 1$, at larger optical depths the external radiation is fully absorbed and has no more influence on the SED. Finally, the dust temperature at the inner boundary of the envelope, T_1 , is adjusted. T_1 has no influence blueward of the SED peak and the shape of the red part of the SED is only affected when T_1 becomes smaller than about 500 K. The LRS spectrum is also very important in determining the correct value of T_1 , as the slope of the LRS spectrum clearly decreases with decreasing values of T_1 .

The optical depth is varied in steps of the order of magnitude of $\tau_{0.5}$, e.g. around $\tau_{0.5} = 50$, also models with $\tau_{0.5} = 40$ and 60 are tried. T_{eff} is varied in steps of 500 K, T_1 in steps of 100 K and the amount of amorphous carbon in steps of 1%. Each model is judged by eye, where equal importance is given to the agreement with the SED and the LRS spectrum. The values from the default model were only altered when this brought along a clear improvement of the fit to the observations.

Two of the sources in our modelling sample, HD 44179 and CPD-56 8032, are said to be surrounded by dusty disks (see respectively Cohen et al. (2004) and de Marco, Barlow & Cohen (2002)), while there is strong evidence that the dust envelopes from VY CMa and 89 Her are not spherically symmetric (see respectively (Josselin et al. 2000) and Waters et al. (1993)). For these sources no acceptable model could be constructed, which is to be expected as DUSTY assumes spherically symmetric mass loss. For one source, IRAS 14331-6435, not enough data were available to con-

strain a model. For all other 18 stars, the SEDs are presented in Appendix A, together with the input parameters and the derived parameters from the DUSTY models. To estimate the errors on the input parameters, we varied one parameter while retaining the values from the best model for the other parameters, until the fit became unacceptable. These errors are clearly only estimates, and not formal errors due to interdependencies of the different parameters.

4.2 Discussion of the SEDs

4.2.1 Quality of the models

In general, the models produced by DUSTY explain the observations quite well, certainly when we keep in mind that a certain scatter of data around the model is to be expected, as our sample stars are variable and the data were taken at different epochs.

There are a few discrepancies that occur in several SEDs. For IRAS 15194-5115, R Hya, α Her and IRC+10 420, the observations at visual and/or near infrared wavelengths can not be explained by the models. For IRC+10 216, this problem was solved by increasing the size of the dust grains, but this does not work for all problematic cases. When the mass loss is small, the spectrum of the central star still has a large influence on the spectrum we observe, especially at short wavelengths. For these cases the discrepancy can be explained by the fact that the central star was modelled with a black body instead of using a stellar spectrum suitable for the central star. That the influence of the central star is not negligible can also be seen from the LRS spectrum, where sometimes the atmospheric absorption by HCN and C_2H_2 can be noticed at $14 \mu\text{m}$.

There are also significant deviations between the observed and modelled submillimetre fluxes. The flux excesses that are seen here, will be discussed in Section 4.2.2. The excess at centimetre wavelengths is discussed separately in Sect. 4.2.3.

4.2.2 Excess at (sub)millimetre wavelengths ($\simeq 100 \mu\text{m} - 1 \text{cm}$)

For almost all of the SEDs, the model provides a good fit for fluxes at wavelengths shorter than about $100 \mu\text{m}$, but for a few of them the longer wavelength fluxes are not in agreement with any of the models that were tested. This is the case for AFGL 1922, IRAS 15194-5115, WX Psc, R Scl and V1300 Aql. In this section, various possible explanations for the observed (sub)millimetre excess will be discussed.

The excess emission at (sub)millimetre wavelengths can be due to molecular line emission, which is not included in the models. IRC+10 216 is known for its rich molecular spectrum. For example, Groenewegen et al. (1997) find an on source contribution from molecular lines which amounts to 43% within the passband of the instrument used, which lies between 220 and 280 GHz and which has an effective frequency of 243 GHz. Nevertheless, the DUSTY-model – which does not include molecular contributions – that was fitted to wavelengths shorter than $500 \mu\text{m}$ explains the (sub)millimetre data for IRC+10 216 well (see Fig. A4). The contribution from molecular lines is too small to necessitate a different model. Our SEDs are plotted using

a log-log scale in units of W m^{-2} so that the SEDs show the physically relevant energy distribution. We conclude that the molecular contribution does not cause a flux excess on the scale used and therefore does not influence the (sub)millimetre modelling. The molecular contribution to the flux will vary from source to source, depending on a variety of factors, such as the dust-to-gas ratio, the temperature and velocity structure in the envelope, etc. However, it is unlikely that these factors will change the order of magnitude of the molecular contribution. The molecular emission is also proportional to the mass-loss rate, which is the best determined parameter of influence. Since IRC+10216 undergoes substantial mass loss, we do not expect the molecular emission to cause a noticeable excess for any other star in the sample, on the scale used in the SED. Therefore, we deem it unlikely that the molecular contribution will cause a substantial effect in the parameters derived from the SED fitting.

The alternative explanation for the observed excesses is an increased amount of dust radiation in the (sub)millimetre range, either (1) because the dust grains radiate more readily at these wavelengths than is assumed in the model or (2) because of the presence of more cold dust than in the model. These effects can be caused by (1) the presence of larger dust grains or (2) by an increased amount of dust farther away from the star. We have explored the first possibility by varying the grain size in our models for three test cases: IRAS 15194-5115, R Scl and WX Psc. Starting from the parameter values of the best fitting model with grain size $0.1 \mu\text{m}$, grain sizes equalling 0.2, 0.5, 1, 5, 10 and $50 \mu\text{m}$ were tested. Because larger grains not only influence the shape of the SED, but also shift the SED as a whole redwards, the optical depth was decreased to counteract this effect. For IRAS 15194-5115, no model could satisfactorily reproduce the SED. For the other 2 sources, it was possible to fit the SED, including the (sub)millimetre fluxes, but these models fail to reproduce the LRS spectrum. As an example: a model with $\tau = 5$ and grain size $a = 5 \mu\text{m}$ fits the SED of WX Psc, but the strong features in the LRS spectrum are not reproduced. On the other hand, a model with $\tau = 10$ and $a = 0.75 \mu\text{m}$ reproduces the LRS spectrum, but not the SED. Besides single sized dust grains we also tried models with grain size distributions $n(a) \propto a^{-q}$ for WX Psc. We used a standard power index of 3.5 and a flatter size distribution with power index 2, grain sizes between 0.01 and $10 \mu\text{m}$ and $\tau = 5$ or 10, but the fits are even less satisfactory than for the single sized grain models.

Note that these results imply that a single population of large grains or a grain size distribution including large grains in a spherical configuration can not be invoked to explain the (sub)millimetre excess. It does not exclude the contribution of large grains in general. The presence of an additional shell of large grains can not be modelled with DUSTY. We have used another radiative transfer code, MODUST (Bouwman et al. 2000), to explore the effect of such a shell for WX Psc. We have taken the inner shell from the model derived from SED fitting as presented by Decin et al. (2007) and placed an extra shell with grains of size 1 or $10 \mu\text{m}$ at different positions in the envelope ($Y = 10, 100, 1000$). Our conclusion is that a shell with

larger grains can only make a significant contribution to the SED at (sub)millimetre wavelengths alone, when the shell is placed far from the star. The low dust temperature implies that the shell must contain a relatively large amount of mass, which was modelled in MODUST by increasing the mass-loss rate in the shell. Models with mass-loss variations will be presented in the next paragraph and further discussed in Sect. 4.2.4. Jura, Turner & Balm (1997) have argued that large dust particles formed in a long-lived disk around HD 44179 can produce the observed millimetre continuum, which is in excess of what simple dust models predict. Again, such a non-spherically symmetric configuration in which a region of enhanced density allows large grains to form can not be modelled by DUSTY. Mauron & Huggins (2006) studied the morphology of AGB envelopes by imaging the circumstellar dust in scattered light at optical wavelengths. For V1300 Aql they found no evidence of special structures in the envelope, although the envelope itself has an elliptical and not a spherical shape. WX Psc seems to have a spherically symmetric extended envelope, but a strong axial symmetry close to the star. R Scl has a spherically symmetric detached shell (see González Delgado et al. (2003)), hence this shell is probably the cause of the (sub)millimetre continuum and there is no need to invoke the presence of large grains. Feast, Whitelock & Marang (2003) argue that IRAS 15194-5115 has a quasi spherical dust shell, with small scale irregularities due to the ejection of dust clouds. No information was found on the geometry of the CSE for AFGL 1922. Hence on the basis of observations of the structure of their envelopes, it seems that a nonspherical distribution of large grains is an unlikely scenario at least for V1300 Aql and R Scl.

To test whether the observed excess is due to dust far from the star, we increase the dust density there in the model. The density distribution as calculated from hydrodynamics assumes a constant mass-loss rate and can be approximated by a distribution $\rho(r) \propto r^{-2}$. Besides a calculation from hydrodynamics equations, DUSTY also offers the possibility to define the density structure with the use of power laws. We tested models with ρ as a function of the relative radius y (scaled to the inner radius of the dust envelope) defined as

$$\rho(y) \propto \begin{cases} y^{-2} & 1 \leq y \leq y_1 \\ y^{-p} & y_1 \leq y \leq Y \end{cases}$$

with p equal to 1.5, 1 or 0.5 and y_1 equal to 10, 100 or 1000, i.e. models with a higher mass loss in the past. For AFGL 1922, IRAS 15194-5115, R Scl, WX Psc and V1300 Aql, such a density distribution improved the fit, both for the SED and for the LRS spectrum. The fact that the density distribution from the hydrodynamics equations is not adequate is an indication for non-constant mass loss. This will be further discussed in Section 4.2.4.

We want to mention IRC +20326 here as well. For this source, the hydrodynamical models overestimated the observational fluxes. Models using smaller dust grains ($a = 0.01$ or $0.001 \mu\text{m}$), could not explain the shape of the SED nor the LRS spectrum. The best fit is obtained by using a model with a steeper density distribution $\rho \propto r^{-3}$ in the outer envelope, consistent with a lower mass loss in the past.

The altered density distribution improves the fit to the

data, but it can not explain the feature around 1 mm for AFGL 1922 (see Fig. A1). This feature might also appear in the SED of IRAS 15194-5115 (Fig. A2), but the fewer observations around this wavelength make it difficult to tell. A search for the origin of this feature is beyond the scope of this article, but molecular emission can be excluded due to the size of the excess.

4.2.3 Excess at centimetre wavelengths

On the basis of the agreement between model and observations at centimetre wavelengths, our sample stars can be divided into two groups. For group I, which is the largest group, it was possible to construct models which provide a good overall fit. V Hya is a perfect example of this (see Fig. A13). In group II, the fit at optical and IR wavelengths is very good, but the models can not explain the observations at radio wavelengths. α Her is representative for this group (see Fig. A15). For α Her the fit is reasonably good up until 1.2 mm, the first observations at longer wavelengths are in the centimetre range and these fluxes are underestimated by the model. Although we are only talking about two observations, we do think that this phenomenon is real and not due to for example a bad choice of model parameters. Firstly, this effect can be seen in several SEDs. We see similar excesses for IRC +20 370, WX Psc, α Sco and V Hya. For all of these stars there are only one or two observations at centimetre wavelengths. For α Her and IRC +10 216 the excess is less obvious, but in these cases there are 4, respectively 8 fluxes that lie systematically higher than the model predictions. Secondly, different models over a wide parameter range were tested, but none could provide a better fit than the one shown. We investigated the influence of the different parameters in DUSTY on the resulting models and we found that only the density distribution of the dust can make a significant difference in flux at millimetre and centimetre wavelengths, without affecting the flux at visual and infrared wavelengths. Models with density distributions defined by power laws as explained in Section 4.2.2 were tested; this sometimes improved the fit, but it could never fully explain the observed excess.

In the literature, there are several articles that comment on a similar flux excess for evolved stars. In Skinner & Whitmore (1987), models are constructed for the outer layers of the atmosphere and the dust envelope of the supergiant α Ori. A composite model of photosphere plus chromosphere plus dust emission can explain the flux below 1 mm wavelength, but to explain the excess at millimetre-centimetre wavelengths, yet another component (being a partially ionised wind in combination with areas of infalling ionised material) has to contribute to the flux. In Knapp et al. (1995), radio continuum observations from a sample of 21 evolved stars with high mass-loss rate and an extended CSE are studied, in the hope of detecting new planetary nebulae. For 4 stars, excess emission is detected that is too weak to be attributed to a compact planetary nebula. The authors suggested a partially ionised chromosphere as the source of this emission.

Hence one possible explanation of the excesses we observe is the presence of a chromosphere. α Sco, which is an early M-type supergiant like α Ori, is known to have a chro-

sphere, this is also the case for α Her. The presence of chromospheres in supergiants is widely accepted, however, it is not yet clear if all AGB stars have chromospheres as well. Drake, Linsky & Elitzur (1987) performed a radio-continuum survey of cool M- and C-giants in a search for chromospheric activity. They concluded that at least in some red giants, chromospheres are either absent or they contain so little ionised gas that their optical depth at centimetre wavelengths is less than unity. α Cet, WX Psc, V Hya and IRC +20 370 all fall in this category of cool M- and C-giants. Sometimes these stars are said to have a chromosphere in the literature, but without convincing arguments.

In Sahai, Claussen & Masson (1989) several mechanisms are discussed to explain the centimetre emission from IRC +10 216. They concluded that a simple black body in combination with dust emission from amorphous carbon is not sufficient to explain the observed fluxes. The most probable cause of the excess is an increase in dust emission at the relevant wavelengths, which can be justified if long carbon molecules (such as PAHs) are present in the dust envelope. In Groenewegen (1997), where a model for the circumstellar dust shell of IRC +10 216 is presented, the dust opacity also had to be increased for wavelengths larger than 1 mm. There is free-free emission present as well, this emission is negligible for wavelengths below 5 mm, but does make a significant contribution to the flux at centimetre wavelengths. In this case the free-free emission is not due to a chromosphere, but to a small partially ionised region with temperatures close to that of the photosphere.

In summary, the most probable explanation for IRC +10 216 is an increase in dust emission at centimetre wavelengths as proposed by Sahai, Claussen & Masson (1989), which could be caused by the presence of long carbon molecules (such as PAHs) in the CSE. α Sco and α Her are known to possess a chromosphere, which could explain the excess emission. For α Cet, WX Psc, V Hya and IRC +20 370 there is no clear evidence for the presence of a chromosphere. For V Hya and IRC +20 370, which have a carbon-rich CSE, the same mechanism as for IRC +10 216 might explain the observed excess.

4.2.4 Mass-loss variations

As already mentioned in Section 4.2.1, we propose a less steep density distribution than the one calculated from hydrodynamics to explain the (sub)millimetre fluxes for AFGL 1922, IRAS 15194-5115, R Scl, WX Psc and V1300 Aql. Hofmann et al. (2001) made an elaborate study of WX Psc and they also found that a two component model with an inner constant mass loss region ($\rho \propto r^{-2}$) and an outer region with $\rho \propto r^{-1.5}$ gives a better match to their observations than a one component model with a uniform outflow. The necessity of a density distribution defined by power laws can be seen as an indication for variable mass loss. All five power laws that were fitted indicate that the mass loss has decreased with time.

For IRC +20 326, a steeper density distribution $\rho \propto r^{-3}$ in the outer envelope was necessary to explain the data. This indicates that the mass loss has increased with time. There is one source, AFGL 4106, where the outer radius of the envelope had to be decreased so that the lowest dust

temperature amounts to 42 K instead of 30 K or lower for the other sources. This might indicate that the past mass-loss rate was so low that we can not detect dust at lower temperatures. We were unable to model this source with a steeper density distribution in the outer envelope instead of the density-cutoff.

There are several mechanisms that might cause mass-loss-rate modulations in AGB stars, each one related to quite distinct time scales. Modulations induced by stellar pulsations would display a period of a few hundred days. Thermal pulses occur only once in ten thousand to hundred thousand years. A third timescale of 200 to 1000 years is derived from the separation between the nested shells seen around IRC +10 216 (Mauron & Huggins 1999) and around several (proto-)planetary nebulae. Simis, Icke & Dominik (2001) suggest that the interplay between grain nucleation and wind dynamics leads to quasi-periodic changes in the mass-loss rate on this time scale. Soker (2000) proposes a solar-like magnetic activity cycle as a mechanism to produce the observed geometry of the CSE surrounding these objects.

From the distance where we find the density profile changes, i.e. the place in our model where the break-point occurs, we can get a rough idea of the duration of the constant mass-loss phase. Translating the break-points into time scales using a typical outflow velocity of 10 km s^{-1} , we find dynamical ages between 700 – 20 000 yr, with an average of 3500 yr, taken into account only those sources that show evidence of mass-loss variability. Of course, if the “constant” mass-loss sources are taking into account this average dynamical age will increase substantially since they do not trace variability out to $\sim 80\,000$ yr, i.e., the outer radius in our modelling. These time scales exclude stellar pulsations as a possible cause of the mass-loss-rate changes detected in the SED. The lower limit of the kinematic age is still in agreement with the third timescale mentioned above. However, the concentric shells seen in IRC +10 216 by Mauron & Huggins (1999) that have lead to this timescale, do not leave their mark in the SED (see Fig. A4). This leaves thermal pulses as the most plausible explanation for the observed mass-loss-rate modulations.

We want to stress here the importance of (sub)millimetre observations to determine the correct density distribution. WX Psc is a clear example. Up to $100 \mu\text{m}$, a density distribution determined from hydrodynamics provides a good fit, but the observations at $400 \mu\text{m}$ and 1.2 mm were clearly underestimated by such a model. On the basis of these observations, a power law density distribution was determined that provided a better overall fit. Measurements at centimetre wavelengths can not be used in determining the correct density distribution, because of the excesses seen at these wavelengths, as discussed in Sect. 4.2.3.

A second type of variation in mass loss is indicated by a low dust temperature at the inner boundary of the dust envelope. Under normal circumstances one expects dust to form once the dust condensation temperature is reached. This dust condensation temperature differs for different species of dust, but for silicates and amorphous carbon 1000 K can be seen as a typical value. When a dust temperature of 150 K is necessary to model the SED, as

is the case for AFGL 4106, this means that the dust that dominates the SED has temperatures far below the dust condensation temperature, so it is located at very large distances from the central star. This implies that the past mass-loss rate was far greater than the present mass-loss rate. For AFGL 4106, which is a post-AGB star, the mass loss has stopped and we are dealing with a detached shell.

All in all, it is not possible to derive detailed information on variations in the mass-loss rate from the SED alone. First of all, DUSTY contains a variety of input parameters and the models presented here are probably degenerate. To determine the correct model for a given star, as many input parameters as possible should be determined in an independent way. With interferometric techniques for example, the inner radius of the dust envelope can be determined, and thus the temperature at the inner edge. Secondly, the physics in DUSTY can be further improved. In the current version there is no way to model two dust shells with each a constant, but different mass-loss rate. Of course, this would even further increase the level of degeneracy of the models. We can conclude that the SED can indicate variations in mass-loss rate, but it should be seen as a basis for further analysis of the object and not as a final stage of the study.

5 VARIABILITY AT 1.2 mm

Several sources were observed during 2 different observation runs. Only 2 of those sources, being α Sco and WX Psc, were strong enough to produce a flux above the detection limit of SIMBA.

From Table 3 it can be seen that the 2 fluxes of α Sco agree with each other within the errors. One does not expect to see much variation, as the 2 observations are separated by 310 d, while the period of α Sco is 350 days (Percy et al. 1996).

WX Psc, a Mira variable with a period in the Johnson K band of 660 d (Samus et al. 2004), does show a clear flux variation. If we take our 2 observations to be coincident with minimum and maximum light, we find an amplitude of 85.1 mJy and a relative variation (the ratio between the amplitude and the average flux at 1.2 mm) of 34 %. This constitutes a lower limit to the true amplitude at 1.2 mm. In Table 4 observations at 1.3 mm are listed that were obtained with the SEST bolometer between March 1992 and March 1994 (Omont, private communication). If we shift these measurements to 1.2 mm, correcting the flux with a power law that was fitted to our model of WX Psc between 1.1 and 1.4 mm

$$F_{\nu \text{ at } 1.2 \text{ mm}} = F_{\nu} \left(\frac{\lambda[\text{mm}]}{1.2} \right)^{4.3}$$

we find values of 86.1 and 80.4 mJy. This points towards an even larger amplitude and relative variation. In the literature, there is not much information to be found on flux variations at such long wavelengths. We mention here a result on the variability of IRC +10 216, because it is also a Mira variable. In Sandell (1994) a figure is shown of the light curve at 1.1 mm. We searched for a period in these data using Fourier analysis and we found 655.3 d as a period from the Lomb-Scargle periodogram. A fit with the following sine

Table 4. Fluxes at 1.3 mm from WX Psc and IRC +10 216 that were obtained between March 1992 and March 1994 with the SEST bolometer (Omont, private communication). No errors were derived.

Name	flux (mJy)	epoch (JD)
WX Psc	61	2448891
	57	2448941
IRC +10 216	2218	2448695
	2363	2448764
	2073	2448942
	1540	2449070
	1327	2449164
	2417	2449315
	1965	2449440

function

$$S(\text{mJy}) = 2329.9 + 362.1 \sin\left(2\pi \frac{JD - 2447301}{655}\right)$$

has a variance reduction of 79%. Here, the relative variation is 16%. From these values we have to conclude that the relative variation found for WX Psc at 1.2 mm is rather large. We also analysed the 1.3 mm data from IRC +10 216 that are listed in Table 4. We fitted a sine function with the period found at 1.1 mm, this gives a variance reduction of 77% and a relative variation of 25%, which is about 10% larger than the relative variation at 1.1 mm. Molecular line emission could explain this difference, as it contributes significantly to the flux at 1.2-1.3 mm: as already mentioned in Sect. 4.2.2, Groenewegen et al. (1997) find an on source contribution from molecular lines of 43%. If the molecular line emission is variable, the observed variations are a superposition of the variations in the dust emission and in the molecular line emission. The larger relative amplitudes at 1.3 mm could be caused by variability in the molecular line emission. As the contribution to the flux from molecular lines within the 1.2 mm SIMBA passband is significant, this could also explain the large relative amplitude for WX Psc at 1.2 mm.

6 CONCLUSIONS

AGB mass loss undergoes variations on different time scales. In this article, we have addressed the question whether these variations also leave their signature in the SED. In order to find the answer, models for the SEDs were presented for a sample which contained mostly AGB stars. As there are few observations available in the millimetre wavelength area, the selected targets were observed at 1.2 mm with SIMBA.

The presented models were constructed with DUSTY. Although there are some discrepancies between observations and model that occur in several SEDs, there is a good overall agreement between models and observations. Five out of 18 sources show a flux excess at (sub)millimetre wavelengths. A modified density distribution compared to a constant mass-loss rate, expressed in terms of power laws and indicative of mass-loss variability, improves the agreement for all five sources. This is why we propose that these five stars have experienced such strong variations in their mass

loss that this is detectable in their SED in the form of a (sub)millimetre excess. The density distributions that were finally used to model these sources, show that the mass-loss rate was higher in the past for all five stars. The presence of large grains in areas with increased density due to asymmetries in the dust envelope can not be ruled out as an alternative explanation, although observations of R Scl and V1300 Aql show no such asymmetries in the envelopes of these stars. One other source, IRC +20326, required a density distribution which implies a lower mass-loss rate in the past. Besides these altered density distributions, a second indication for variations in the mass loss can be found in a dust temperature at the inner boundary of the dust envelope that lies far below the dust condensation temperature, which indicates the presence of a detached shell. We conclude that the SED can contain clear indications for variable mass loss, but that it is not possible to derive detailed information on the basis of the SED alone. This is due to the uncertainties on the many free parameters in the DUSTY models and because there are not many options in DUSTY to adequately model a variable mass loss.

We also analysed the time variability in our 1.2 mm data for α Sco and WX Psc, which were observed during two different observation runs. We found that WX Psc shows a relative variation of at least 34%, which is rather large when compared to the relative variation of 16% for IRC +10 216 at 1.1 mm. We propose that a contribution to the flux from variable molecular line emission might explain the large relative variation of WX Psc at 1.2 mm.

ACKNOWLEDGEMENTS

SD and LD acknowledge financial support from the Fund for Scientific Research - Flanders (Belgium), SH acknowledges financial support from the Interuniversity Attraction Pole of the Belgian Federal Science Policy P5/36.

REFERENCES

- Arenou F., Grenon M., Gomez A., 1992, *A&A*, 258, 104
- Bouwman J., de Koter A., van den Ancker M.E., Waters L.B.F.M., 2000, *A&A*, 360, 213
- Cohen M. et al., 1975, *ApJ*, 196, 179
- Cohen M., Van Winckel H., Bond H.E., Gull T.R., 2004, *AJ*, 127, 2362
- Decin L., Hony S., de Koter A., Molenberghs G., 2007, *A&A*, in preparation
- de Marco O., Barlow M.J., Storey P.J., 1997, *MNRAS*, 292, 86
- de Marco O., Barlow M.J., Cohen M., 2002, *ApJ*, 574, L83
- Draine B.T., Lee H.M., 1984, *ApJ*, 285, 89
- Drake S.A., Linsky J.L., Elitzur M., 1987, *AJ*, 94, 1280
- ESA, 1997, *VizieR Online Data Catalog*, I/239
- Feast M.W., Whitelock P.A., Marang F., 2003, *MNRAS*, 346, 878
- González Delgado D., Olofsson H., Schwarz H.E., Eriksson K., Gustafsson B., Gledhill T., 2003, *A&A*, 399, 1021
- Groenewegen M.A.T., 1997, *A&A*, 317, 503
- Groenewegen M.A.T., de Jong T., Baas F., 1993, *A&AS*, 101, 513

Groenewegen M.A.T., van der Veen W.E.C.J., Lefloch B., Omont A., 1997, *A&A*, 322, L21
 Habing H.J., 1996, *A&AR*, 7, 97
 Hanner M.S., 1988, NASA Conference Publications, 3004, 22
 Harvey P.M., Bechis K.P., Wilson W.J., Ball J.A., 1974, *ApJS*, 27, 331
 Hofmann K.H., Balega Y., Blöcker T., Weigelt G., 2001, *A&A*, 379, 529
 Ivezić Z., Elitzur M., 1997, *MNRAS*, 287, 799
 Ivezić Z., Nenkova M., Elitzur M., 1999, User Manual For Dusty, University of Kentucky, <http://www.pa.uky.edu/~moshe/dusty>
 Jenness T., Stevens J.A., Archibald E.N., Economou F., Jessop N.E., Robson E.I., 2002, *MNRAS*, 336, 14
 Jones T.J. et al., 1993, *ApJ*, 411, 323
 Josselin E., Blommaert J.A.D.L., Groenewegen M.A.T., Omont A., Li F.L., 2000, *A&A*, 357, 225
 Josselin E., Lèbre A., 2001, *A&A*, 367, 826
 Jura M., Chen C., Werner M.W., 2000a, *ApJ*, 541, 264
 Jura M., Chen C., Werner M.W., 2000b, *ApJ*, 544, L141
 Jura M., Turner J., Balm S.P., 1997, *ApJ*, 474, 741
 Knapp G.R., Bowers P.F., Young K., Phillips T.G., 1995, *ApJ*, 455, 293
 Kwok S., Volk K., Bidelman W.P., 1997, *ApJS*, 112, 557
 Loup C., Forveille T., Omont A., Paul J.F., 1993, *A&AS*, 99, 291
 Mauron N., Huggins P.J., 1999, *A&A*, 349, 203
 Mauron N., Huggins P.J., 2006, *A&A*, 452, 257
 Molster F.J. et al., 1999, *A&A*, 350, 163
 Observers handbook SIMBA, 2003, edition 1.9, <http://www.ls.eso.org/lasilla/Telescopes/SEST/html/telescope-instruments/simba>
 Ossenkopf V., Henning T., Mathis J.S., 1992, *A&A*, 261, 567
 Pégourié B., 1988, *A&A*, 194, 335
 Percy J.R., Desjardins, A., Yu L., Landis H.J., 1996, *PASP*, 108, 139
 Ryde N., Schöier F.L., Olofsson H., 1999, *A&A*, 345, 841
 Sahai R., Claussen M.J., Masson C.R., 1989, *A&A*, 220, 92
 Samus N.N. et al., 2004, *VizieR Online Data Catalog*, II/250
 Sandell G., 1994, *MNRAS*, 271, 75
 Savage B.D., Mathis J.S., 1979, *ARA&A*, 17, 73
 Schöier F.L., Lindqvist M., Olofsson H., 2005, *A&A*, 436, 633
 Simis Y.J.W., Icke V., Dominik C., 2001, *A&A*, 371, 205
 Skinner C.J., Whitmore B., 1987, *MNRAS*, 224, 335
 Soker N., 2000, *ApJ*, 540, 436
 van der Veen W.E.C.J., Omont A., Habing H.J., Matthews H.E., 1995, *A&A*, 295, 445
 Vassiliadis E., Wood P.R., 1993, *ApJ*, 413, 641
 Waters L.B.F.M., Waelkens C., Mayor M., Trams N.R., 1993, *A&A*, 269, 242

fitting models. The caption of Fig. A1 contains the explanation of the symbols used, for all other figures only the model parameters are given. We comment here on some discrepancies between LRS spectrum and model that have not already been discussed in the article. Several LRS spectra show signs of the atmospheric absorption by HCN and C₂H₂ at 14 μ m. This is the case for IRAS 15194-5115, AFGL 3068, IRC +10 216 and R Scl. At 8 μ m the signature of the SiO fundamental band is visible in the spectra of *o* Cet, IK Tau, R Hya, W Hya and α Sco. In the spectrum of AFGL 3068, SiC goes into self absorption around 12 μ m, which we should be able to model with a larger optical depth. However, a larger value of $\tau_{0.5}$ degrades the quality of the fit to the SED and to the wings of the LRS. This apparent contradiction could indicate a non-spherical mass loss. The discrepancies between LRS spectrum and model for R Scl are mainly caused by molecular absorption by HCN at 8 μ m and around 14 μ m in combination with C₂H₂. The spectrum of R Hya shows a strong molecular band from H₂O to the left of the silicate feature at 9.7 μ m. And the discrepancy between the model and the blue wing of the LRS for AFGL 4106 and IRC +10 420 is probably caused by a lack of Fe in the model.

APPENDIX A: DUST MODELS

Table A1 gives an overview of the input parameters used for the models, Table A2 does the same for the parameters that were derived from the models. Figures A1 to A18 show the SEDs and the LRS spectra together with the best

Table A1. This table gives an overview of the input parameters used for the models. A_v is the interstellar reddening derived from the model of Arenou, Grenon & Gomez (1992), $\tau_{0.5}$ is the optical depth at $0.5 \mu\text{m}$, T_{eff} is the effective temperature of the central black body and T_1 is the dust temperature at the inner boundary of the dust envelope. When no error is given for T_{eff} or T_1 , this means that the temperature is undetermined. The oxygen rich dust composition is undetermined when $\tau_{0.5} \leq 0.1$, except in the case of α Sco. The last column lists any other parameters that were altered with respect to the default model (see Sect. 4.1): density structure with parameters p and y_1 , relative outer radius of the envelope Y or grain size a . For Y , only the order of magnitude is determined.

Name	A_v	$\tau_{0.5}$	T_{eff} (K)	T_1 (K)	dust composition	other parameters
AFGL 1922	0.98 ± 0.54	50^{+30}_{-30}	2500	1200^{+500}_{-100}	AMC= 93 \pm 3 %	$p = 1.5 \pm 0.3$ beyond $y_1 = 100$
IRAS 15194-5115	0.59 ± 0.32	15^{+15}_{-5}	2500	900^{+100}_{-100}	AMC= 96 \pm 2 %	$p = 1.5 \pm 0.3$ beyond $y_1 = 100$
AFGL 3068	0.15 ± 0.15	80^{+5}_{-5}	2500	600^{+100}_{-100}	AMC= 93 \pm 5 %	
IRC +10 216	0.06 ± 0.15	15^{+5}_{-5}	2500	600^{+100}_{-100}	AMC= 97 \pm 2 %	$a = 0.15 \pm 0.05$
IRC +20 370	0.49 ± 0.20	10^{+5}_{-5}	2500	900^{+200}_{-200}	AMC= 90 \pm 2 %	
V Hya	0.16 ± 0.15	3^{+2}_{-2}	2500	700^{+200}_{-200}	AMC= 93 \pm 2 %	
R Scl	0.00 ± 0.15	$0.5^{+0.2}_{-0.3}$	2500^{+500}_{-500}	1000^{+300}_{-200}	AMC= 90 \pm 5 %	$p = 1 \pm 0.2$ beyond $y_1 = 100$
IRC +20 326	0.32 ± 0.15	20^{+10}_{-10}	2500	700^{+100}_{-200}	AMC= 97 \pm 2 %	$p = 3 \pm 0.4$ beyond $y_1 = 100$
o Cet	0.07 ± 0.16	$1^{+1}_{-0.9}$	3000^{+500}_{-750}	1000^{+300}_{-300}	SilOc	
IK Tau	0.32 ± 0.17	20^{+10}_{-5}	2500	1000^{+200}_{-200}	SilDL	$a = 0.15 \pm 0.1$
WX Psc	0.12 ± 0.17	70^{+10}_{-20}	2500	1000^{+200}_{-100}	SilOw	$p = 1.5 \pm 0.4$ beyond $y_1 = 100$
R Hya	0.23 ± 0.15	$0.1^{+0.4}_{-0.09}$	2500^{+500}_{-500}	300^{+100}_{-100}	SilDL	
W Hya	0.20 ± 0.15	$0.1^{+0.9}_{-0.09}$	2000^{+500}_{-500}	1000	SilDL	
V1300 Aql	0.46 ± 0.26	50^{+10}_{-10}	2500	1000^{+200}_{-100}	SilOc	$p = 1.5 \pm 0.3$ beyond $y_1 = 100$
α Her	0.28 ± 0.17	$0.01^{+0.09}_{-0.009}$	3000^{+500}_{-500}	1000	SilDL	
AFGL 4106	1.34 ± 0.67	5^{+3}_{-2}	7000	150^{+50}_{-50}	SilOw	$Y = 10^{+10}_{-5}$
α Sco	0.76 ± 0.40	$0.1^{+0.1}_{-0.05}$	3000^{+1000}_{-500}	1000^{+400}_{-400}	SilDL	
IRC +10 420	1.96 ± 1.03	10^{+5}_{-5}	7000	400	SilOw	

Table A2. This is an overview of the output parameters of the presented models. L is the luminosity, r_1 is the distance between the dust envelope and the central star, r_1/r_c is the ratio of this distance to the radius of the central star. The hydrodynamics calculations give a value for the mass-loss rate \dot{M} and the terminal outflow velocity V_e . If the terminal outflow velocity falls below 5 km s^{-1} , the values of \dot{M} and V_e can not be trusted (indicated with an exclamation mark), if T_{eff} drops below a critical temperature inherent to the model, all values listed in the table are uncertain (indicated with an asterisk).

Name	L (L_{\odot})	\dot{M} ($M_{\odot} \text{ yr}^{-1}$)	V_e (km s^{-1})	r_1 (cm)	r_1/r_c
AFGL 1922	$1.03 \cdot 10^4$			$2.15 \cdot 10^{14}$	5.71
IRAS 15194-5115	$1.17 \cdot 10^4$			$4.07 \cdot 10^{14}$	10.2
AFGL 3068 !	$6.78 \cdot 10^3$	$3.34 \cdot 10^{-5}$	4.85	$9.47 \cdot 10^{14}$	31.1
IRC +10 216	$7.87 \cdot 10^3$	$1.73 \cdot 10^{-5}$	6.65	$1.03 \cdot 10^{15}$	31.3
IRC +20 370	$1.12 \cdot 10^4$	$7.87 \cdot 10^{-6}$	15.1	$3.90 \cdot 10^{14}$	9.92
V Hya	$9.78 \cdot 10^3$	$4.72 \cdot 10^{-6}$	13.0	$6.65 \cdot 10^{14}$	18.1
R Scl	$1.32 \cdot 10^4$			$2.80 \cdot 10^{14}$	6.57
IRC +20 326	$8.82 \cdot 10^3$			$6.84 \cdot 10^{14}$	19.6
o Cet	$1.06 \cdot 10^4$	$1.15 \cdot 10^{-6}$	16.2	$2.03 \cdot 10^{14}$	7.63
IK Tau *	$1.06 \cdot 10^4$	$8.23 \cdot 10^{-6}$	14.1	$2.38 \cdot 10^{14}$	6.26
WX Psc	$7.38 \cdot 10^3$			$2.35 \cdot 10^{14}$	7.36
R Hya !	$1.03 \cdot 10^4$	$3.57 \cdot 10^{-7}$	3.05	$1.07 \cdot 10^{15}$	28.2
W Hya *	$1.26 \cdot 10^4$	$1.07 \cdot 10^{-7}$	7.11	$1.37 \cdot 10^{14}$	2.10
V1300 Aql	$9.51 \cdot 10^3$			$2.34 \cdot 10^{14}$	6.46
α Her	$2.04 \cdot 10^4$	$5.09 \cdot 10^{-8}$	7.16	$2.16 \cdot 10^{14}$	5.86
AFGL 4106 !	$2.48 \cdot 10^5$	$9.50 \cdot 10^{-4}$	3.73	$1.81 \cdot 10^{17}$	$7.68 \cdot 10^3$
α Sco	$7.98 \cdot 10^4$	$1.41 \cdot 10^{-7}$	10.1	$4.27 \cdot 10^{14}$	5.86
IRC +10 420	$2.88 \cdot 10^5$	$4.78 \cdot 10^{-4}$	10.0	$2.21 \cdot 10^{16}$	$8.71 \cdot 10^2$

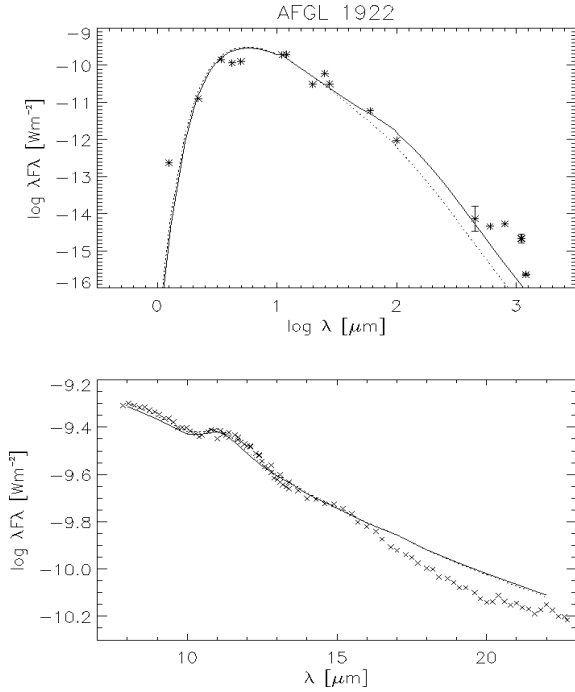


Figure A1. $T_1 = 1200$ K, AMC = 93 %, $\tau_{0.5} = 50$, $T_{\text{eff}} = 2500$ K, $\rho(y) \propto y^{-2}$ between $Y = 1$ and $Y = 100$, $\rho(y) \propto y^{-1.5}$ between $Y = 100$ and $Y = 5000$. The upper figure shows the photometric data (asterisk) and the model (full line). Error-bars are shown, but most of the time they fall within the symbols. A reversed triangle represents an upper limit. The lower figure shows the LRS spectrum (plus signs) and the model (full line). As a comparison, the dotted line shows the corresponding hydrodynamical model.

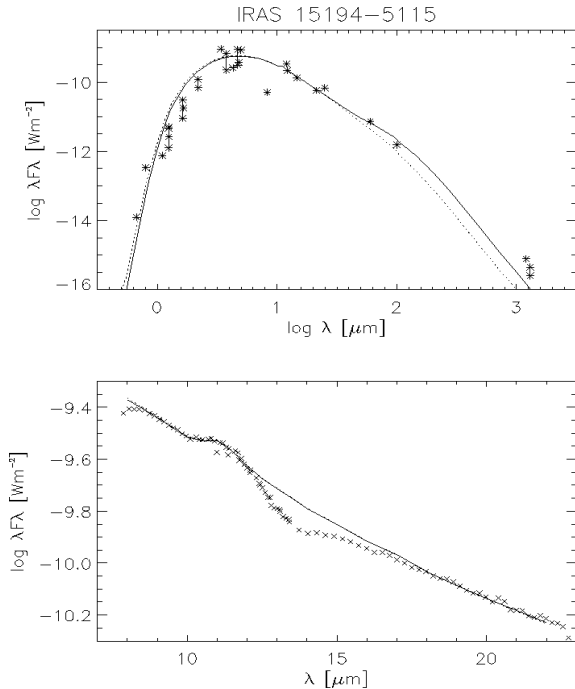


Figure A2. $T_1 = 900$ K, AMC = 96 %, $\tau_{0.5} = 15$, $T_{\text{eff}} = 2500$ K, $\rho(y) \propto y^{-2}$ between $Y = 1$ and $Y = 100$, $\rho(y) \propto y^{-1.5}$ between $Y = 100$ and $Y = 5000$.

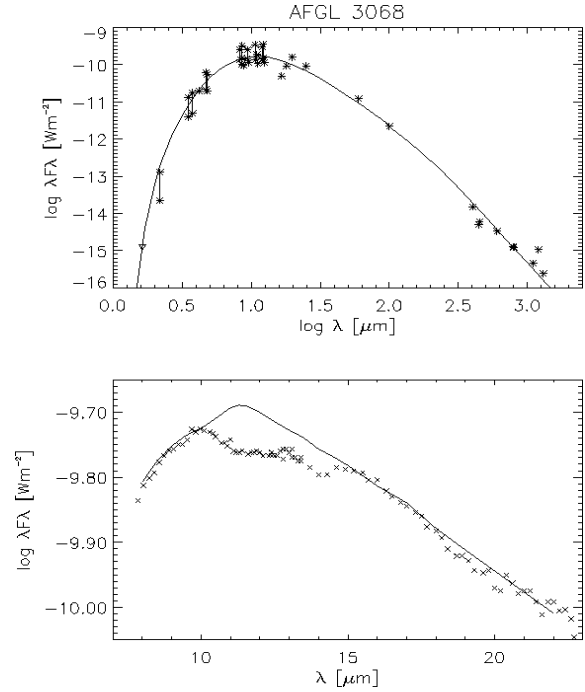


Figure A3. $T_1 = 600$ K, AMC = 93 %, $\tau_{0.5} = 80$, $T_{\text{eff}} = 2500$ K.

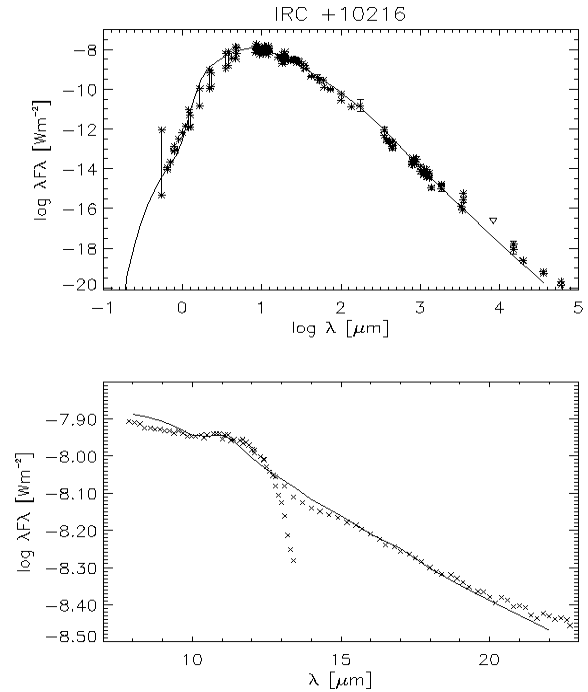


Figure A4. $T_1 = 600$ K, AMC = 97 %, $\tau_{0.5} = 15$, $T_{\text{eff}} = 2500$ K, $a = 0.15 \mu\text{m}$.

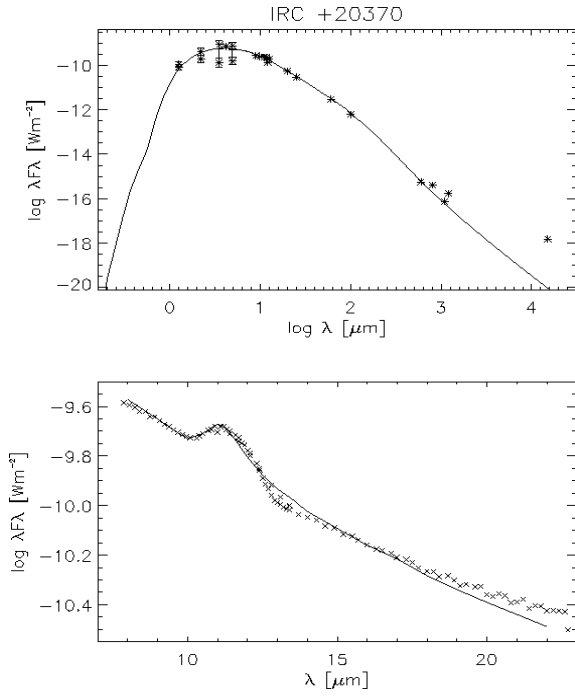


Figure A5. $T_1 = 900$ K, AMC = 90 %, $\tau_{0.5} = 10$, $T_{\text{eff}} = 2500$ K.

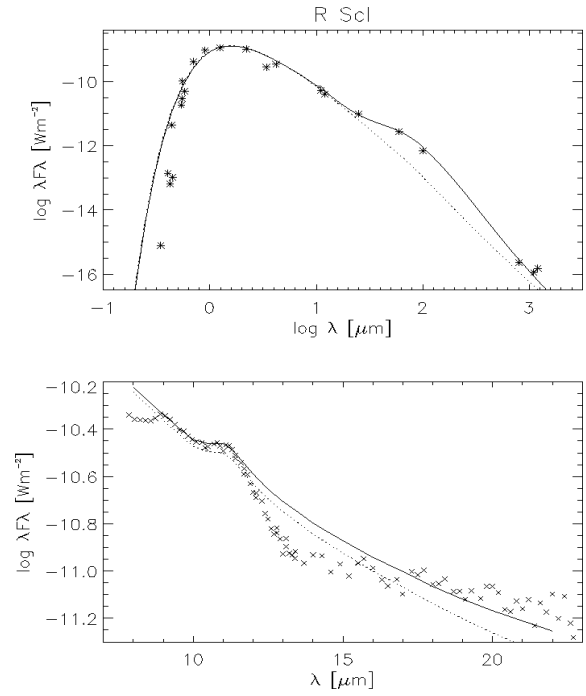


Figure A7. $T_1 = 1000$ K, AMC = 90 %, $\tau_{0.5} = 0.5$, $T_{\text{eff}} = 2500$ K, $\rho(y) \propto y^{-2}$ between $Y = 1$ and $Y = 100$, $\rho(y) \propto y^{-1}$ between $Y = 100$ and $Y = 5000$.

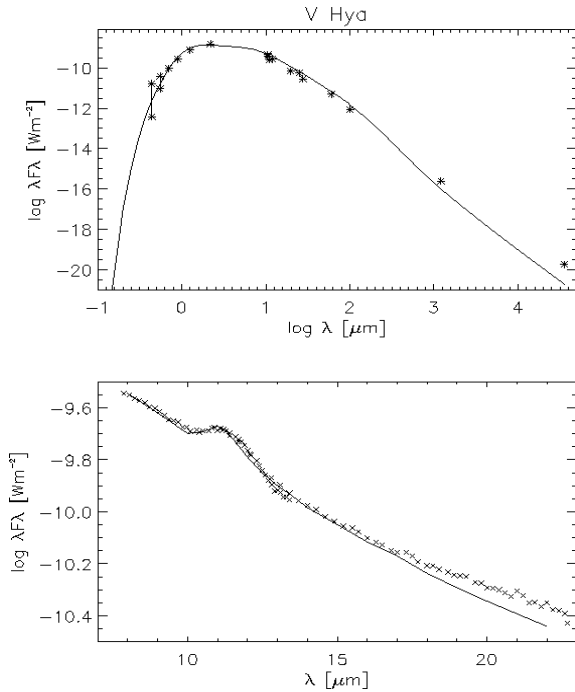


Figure A6. $T_1 = 700$ K, AMC = 93 %, $\tau_{0.5} = 3$, $T_{\text{eff}} = 2500$ K.

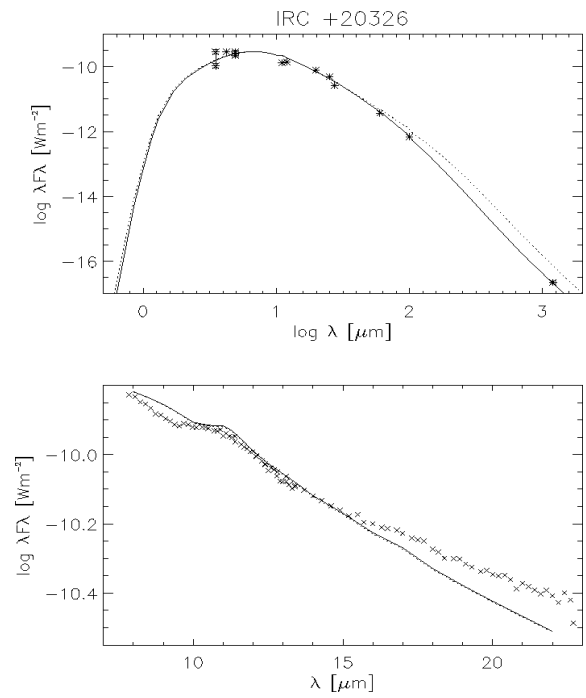


Figure A8. $T_1 = 700$ K, AMC = 97 %, $\tau_{0.5} = 20$, $T_{\text{eff}} = 2500$ K, $\rho(y) \propto y^{-2}$ between $Y = 1$ and $Y = 100$, $\rho(y) \propto y^{-3}$ between $Y = 100$ and $Y = 5000$.

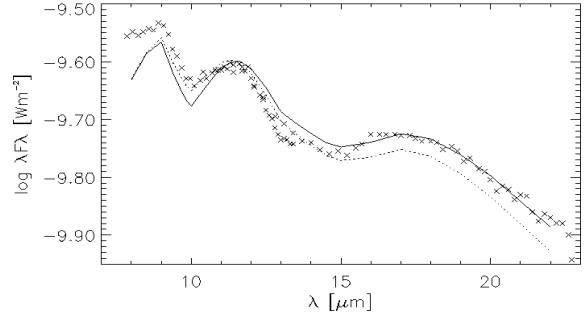
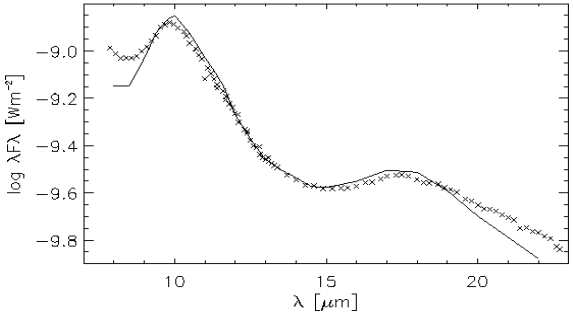
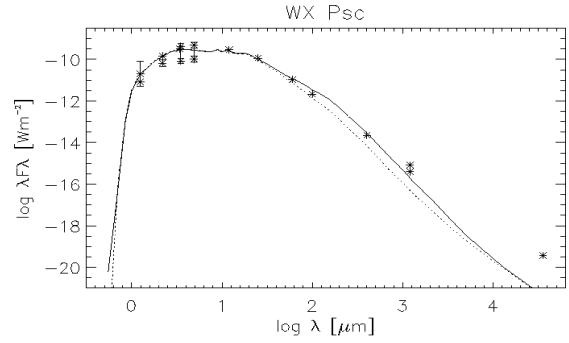
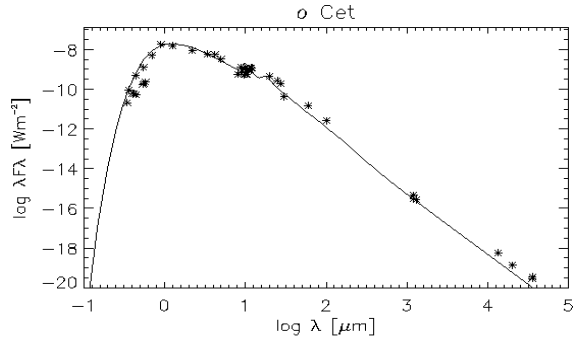


Figure A9. $T_1 = 1000$ K, SilOc, $\tau_{0.5} = 1$, $T_{\text{eff}} = 3000$ K.

Figure A11. $T_1 = 1000$ K, SilOw, $\tau_{0.5} = 70$, $T_{\text{eff}} = 2500$ K, $\rho(y) \propto y^{-2}$ between $Y = 1$ and $Y = 100$, $\rho(y) \propto y^{-1.5}$ between $Y = 100$ and $Y = 5000$.

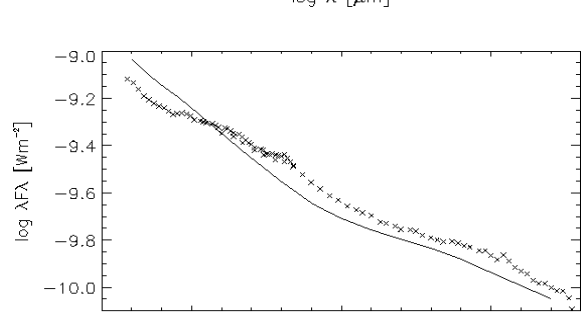
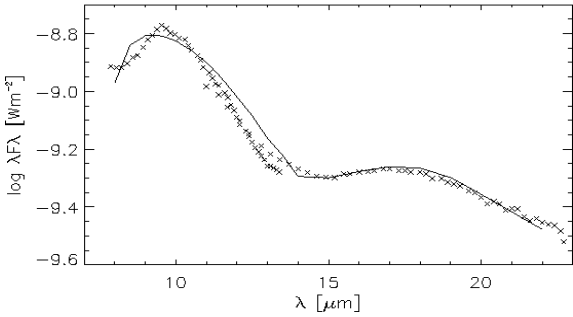
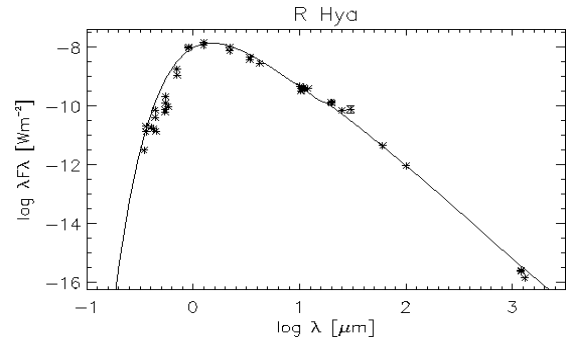
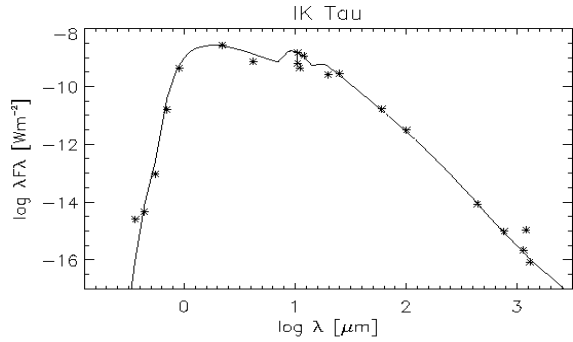


Figure A10. $T_1 = 1000$ K, SilDL, $\tau_{0.5} = 20$, $T_{\text{eff}} = 2500$ K, $a = 0.15 \mu\text{m}$.

Figure A12. $T_1 = 300$ K, SilDL, $\tau_{0.5} = 0.1$, $T_{\text{eff}} = 2500$ K.

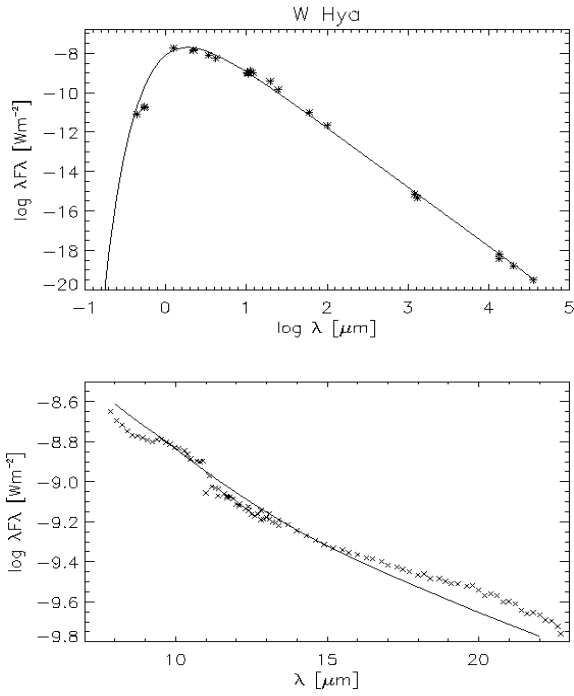


Figure A13. $T_1 = 1000$ K, SilDL, $\tau_{0.5} = 0.1$, $T_{\text{eff}} = 2000$ K.

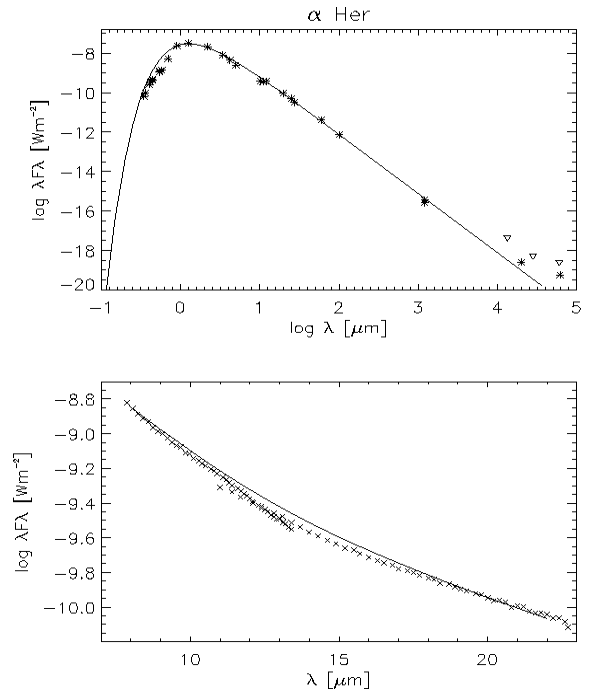


Figure A15. $T_1 = 1000$ K, SilDL, $\tau_{0.5} = 0.01$, $T_{\text{eff}} = 3000$ K.

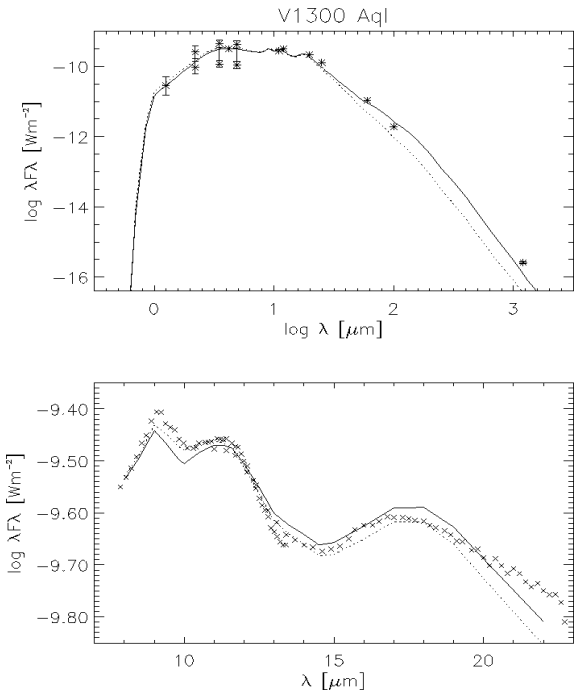


Figure A14. $T_1 = 1000$ K, SilOc, $\tau_{0.5} = 50$, $T_{\text{eff}} = 2500$ K, $\rho(y) \propto y^{-2}$ between $Y = 1$ and $Y = 100$, $\rho(y) \propto y^{-1.5}$ between $Y = 100$ and $Y = 5000$.

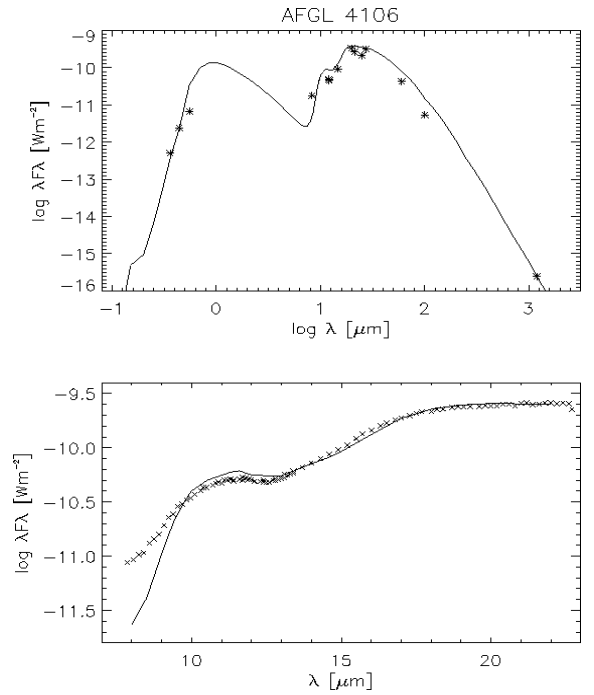


Figure A16. $T_1 = 150$ K, SilOw, $\tau_{0.5} = 5$, $T_{\text{eff}} = 7000$ K, $Y = 10$.

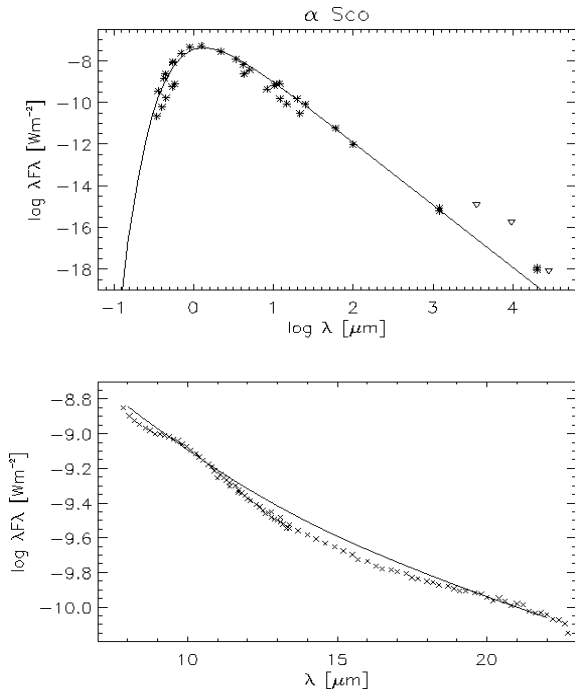


Figure A17. $T_1 = 1000$ K, SilDL, $\tau_{0.5} = 0.1$, $T_{\text{eff}} = 3000$ K.

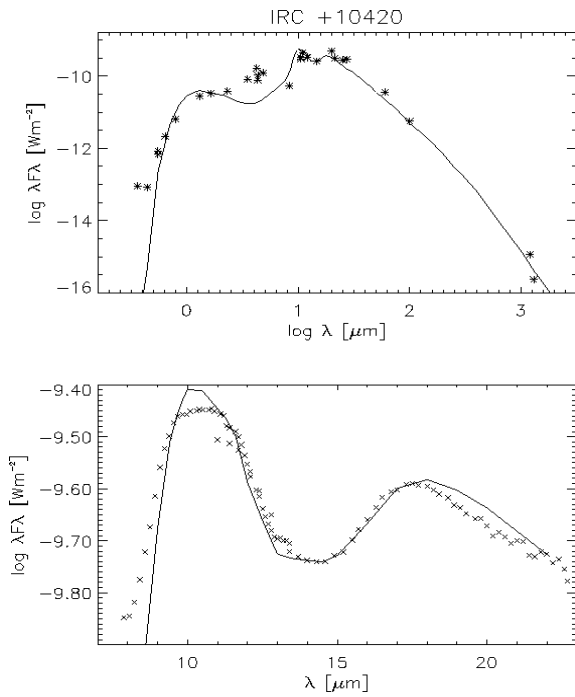


Figure A18. $T_1 = 400$ K, SilOw, $\tau_{0.5} = 10$, $T_{\text{eff}} = 7000$ K.